Effects of convex transverse curvature on wall-bounded turbulence. Part 2. The pressure fluctuations

By JOÃO C. NEVES[1]† AND PARVIZ MOIN[1,2]

[1] Department of Mechanical Engineering, Stanford University, Stanford, CA 94305, USA

[2] NASA Ames Research Center, Moffett Field, CA 94035, USA

The effects of convex transverse curvature on the wall pressure fluctuations were studied through direct numerical simulations. The flow regime of interest is characterized by large ratio of the shear-layer thickness to the radius of curvature ($\gamma = \delta/a$) and by small a^+, the radius of curvature in wall units. Two direct numerical simulations of a model problem approximating axial flow boundary layers on long cylinders were performed for $\gamma = 5$ ($a^+ \approx 43$) and $\gamma = 11$ ($a^+ \approx 21$). The space–time characteristics of the wall pressure fluctuations of the plane channel flow simulation of Kim, Moin & Moser (1987), which were studied by Choi & Moin (1990) are used to assess the effects of curvature.

As the curvature increases the root-mean-square (r.m.s.) pressure fluctuations decrease and the ratio of the streamwise to spanwise lengthscales of the wall pressure fluctuations increases. Fractional contributions from various layers in the flow to the wall r.m.s. pressure fluctuations are marginally affected by the curvature. Curvature-dependent timescales and lengthscales are identified that collapse the high-frequency range of the wall pressure temporal spectra and the high wave-number range of the wall pressure streamwise spectra of flows with different curvatures. Taylor's hypothesis holds for the wall pressure fluctuations with a lower convection velocity than in the planar case.

1. Introduction

Knowledge of the characteristics of the wall pressure fluctuations is important for understanding fluid/structure interactions and hydro-acoustics. A comprehensive treatment of this subject is given by Blake (1986). Wall pressure fluctuations affect the acoustic characteristics (both radiation and detection) of underwater vehicles. Transversely curved turbulent flows occur over sonar devices towed by long cables; in such cases it is important to understand the characteristics of the wall pressure fluctuations in the flow regime where $\gamma = \delta/a$ is large and $a^+ = au_\tau/\nu$ is small. Here, δ is the boundary-layer thickness, a is the cylinder radius, $u_\tau = (\tau_w/\rho)^{1/2}$ is the shear velocity, ν is the kinematic viscosity and τ_w is the mean wall shear stress. For this flow regime (large γ and small a^+) there is only limited experimental data available on the statistical properties of the wall pressure fluctuations. Reviews of the experimental data of the wall pressure fluctuations on a flat plate are given by Willmarth (1975) and Eckelmann (1989). The effects of transverse curvature on the space–time characteristics of the wall pressure were investigated experimentally by Willmarth & Yang (1970) for

† Present address: Naval Research Laboratory, Washington DC 20375-7220, USA.

$\gamma \approx 2$ and by Willmarth *et al.* (1976) for $\gamma \approx 4$. Since in both studies $a^+ = O(10^3)$, the curvature effects were limited to the outer part of the flow.

Many of the difficulties in the measurement of the wall pressure fluctuations are avoided in direct numerical simulations (Handler *et al.* 1984; Choi & Moin 1990). However, simulations are limited to low Reynolds numbers. There is evidence (Willmarth 1975; Choi & Moin 1990) that the r.m.s. pressure normalized by the mean wall shear decreases with decreasing Reynolds number. Choi & Moin (1990) also found that the spectrum of the wall pressure fluctuations decreases with decreasing Reynolds number for low frequencies when scaled with inner variables, and for high frequencies when scaled with the outer variables. In measurements of the wall pressure intensity in a transversely curved boundary layer Willmarth & Yang (1970) concluded that the transverse curvature did not have a significant effect. However, this result is for a mild transverse curvature ($\gamma \simeq 2, a^+ \simeq 4500$), in which only the outer part of the boundary layer was affected by the curvature. In addition, any small curvature dependence that was present in their study was probably overshadowed by the strong Reynolds-number dependence of the wall pressure intensity. In subsequent wall pressure measurements on a cylinder (Willmarth *et al.* 1976), for which $\gamma \simeq 4$, the value of the wall r.m.s. pressure was not reported.

As had been found in previous experiments (Willmarth & Wooldridge 1962; Wills 1964; Emmerling, Meier & Dinkelacker 1973), the large-scale pressure correlation contours of Choi & Moin (1990) were more elongated in the spanwise direction than in the streamwise direction. However, the effect of curvature on the spatial correlations of the wall pressure correlations has not been established. Willmarth & Yang (1970) ($\gamma \approx 2$) suggest that for large separations the ratio of spanwise to streamwise lengthscales decreases. However, their later study for $\gamma \approx 4$ (Willmarth *et al.* 1976) shows the opposite trend. Nevertheless, the wall pressure is significantly correlated around the cylinder and the azimuthal extent of the correlation increases with increasing curvature (Willmarth *et al.* 1976). Willmarth & Yang (1970) argued that the main effect of the transverse curvature is to reduce the spanwise lengthscale of the large eddies, located in the outer part of the boundary layer.

In the planar turbulent boundary layer (Willmarth & Wooldridge 1962) as well as in the transversely curved turbulent boundary layer (Willmarth & Yang 1970; Willmarth *et al.* 1976), the space–time wall pressure correlations indicate that the eddies decay after travelling a distance of the order of their size. Convection velocities can be defined from the wall pressure space–time correlation contours (Wills 1964). In the planar geometry, there is a consensus among the experimental (Willmarth & Wooldridge 1962; Panton & Linebarger 1974) and numerical (Choi & Moin 1990) values reported for the convection velocity, which is about $0.8 U_{\infty}$. In the transversely curved turbulent flows of Willmarth & Yang (1970) and Willmarth *et al.* (1976), convection velocities identical to that of the planar case were reported.

The objective of this paper is to examine and document the space–time characteristics of the wall pressure fluctuations in axial turbulent flows over long cylinders. To this end, we consider the direct numerical simulations presented in Neves, Moin & Moser (1993; hereinafter referred to as Part 1). As discussed in Part 1, the simulated flow was the axial flow between concentric cylinders, with no-stress boundary conditions on the outer cylinder, driven by a mild pressure gradient. In this model, some of the features of a free boundary layer developing on a cylinder, which has been studied experimentally, are absent. However, the model does account for the effects of transverse curvature in the absence of additional complications present in the free boundary layer.

For comparison, the spatial and temporal spectra of the plane channel wall pressure fluctuations from a database generated by Kim, Moin & Moser (1987) and Choi & Moin (1990) were used. The Reynolds number of the plane channel flow and that of the present flows are similar, and thus differences in the statistical characteristics can be ascribed to the transverse curvature alone.

The width of the gap between the cylinders corresponds roughly to the thickness of a boundary layer and is denoted by δ, and the curvature parameter is $\gamma = \delta/a$, where a is the inner cylinder radius. Throughout the paper δ and the friction velocity (u_τ) are used for non-dimensionalization, unless otherwise noted. Thus, in these units the radial (r) domain is $r \in [a', a'+1]$, and the curvature parameter is $\gamma = 1/a'$, where $a' = a/\delta$ is the non-dimensional cylinder radius. In the remainder of the paper, the prime will be dropped for simplicity (thus a now refers to the non-dimensional radius). Total fields are indicated by upper case symbols and fluctuating fields are denoted by lower case symbols. For example, V and v are the total and fluctuating velocity vectors, respectively. In the two transverse curvature flow simulations discussed here, z, θ and r are the axial (streamwise), azimuthal (spanwise) and radial coordinates respectively, and y is the radial distance from the cylinder wall $(y = r-a)$. The statistics were obtained from a sample collected after the calculations had reached the statistically steady state, and are calculated by averaging in the θ- and z-directions and time. The wall pressure database on which the results are based was generated after the flow had reached statistical steady state. Additional integration of the governing equations for wall pressure statistics were carried out for a period of 12.8 δ/u_τ in the $\gamma = 5$ flow and 8.6 δ/u_τ in the $\gamma = 11$ flow. The wall pressure was sampled at intervals Δt_s for a total period L_T, resulting in N_s time samples. In the temporal analysis a window of length L_t is used. These parameters are given in table 1 for the three simulations under consideration. The numerical procedure used to compute the space–time characteristics of the wall pressure fluctuations is described in Neves *et al.* (1992) and will not be discussed here.

The effects of transverse curvature on the sources of pressure fluctuations are discussed in §2. Section 3 contains the spatial spectra of the wall pressure fluctuations and in §4 the two-point correlations are presented. The fractional contributions of various flow regions to the wall pressure are studied in §5. The temporal spectra are presented in §6. Finally, §7 treats the convection velocity of the wall pressure fluctuations and examines the validity of Taylor's hypothesis.

2. Pressure source terms

The Poisson equation for the pressure field is obtained from the divergence of the Navier–Stokes equations,

$$\nabla^2 p = -2\frac{\partial \bar{V}_z}{\partial r}\frac{\partial v_r}{\partial z} - \left(\frac{\partial v_r}{\partial r}\right)^2 - \frac{2}{r}\frac{\partial v_\theta}{\partial r}\left(\frac{\partial v_r}{\partial \theta} - v_\theta\right)$$
$$-2\frac{\partial v_z}{\partial r}\frac{\partial v_r}{\partial z} - \frac{1}{r^2}\left(\frac{\partial v_\theta}{\partial \theta} + v_r\right)^2 - \frac{2}{r}\frac{\partial v_z}{\partial \theta}\frac{\partial v_\theta}{\partial z} - \left(\frac{\partial v_z}{\partial z}\right)^2. \quad (1)$$

Boundary conditions for the pressure are obtained by evaluating the radial momentum equation at both boundaries of the finite domain in r,

$$\left.\frac{\partial p}{\partial r}\right|_{r=a} = \frac{1}{Re_\tau}\left.\frac{\partial^2 v_r}{\partial r^2}\right|_{r=a}, \quad \left.\frac{\partial p}{\partial r}\right|_{r=a+1} = \left[-\frac{1}{Re_\tau}\frac{2}{r^2}\frac{\partial v_\theta}{\partial \theta} + \frac{v_\theta^2}{r}\right]_{r=a+1}. \quad (2)$$
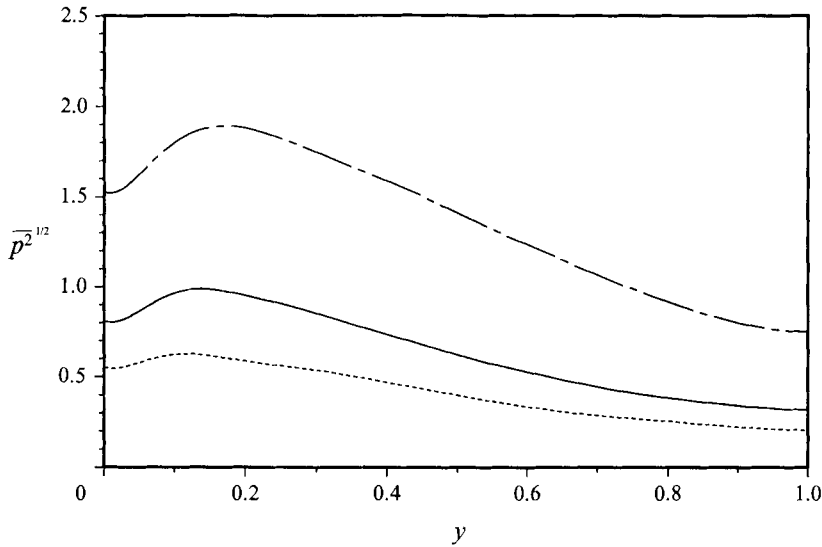
FIGURE 1. Root-mean square pressure in global coordinates: ———, plane channel (Kim 1989); cylinders with ———, $\gamma = 5$ and ————, $\gamma = 11$.

γ	0	5	11
L_T	9.36	12.9	8.6
L_t	1.20	0.806	0.659
Δt_s	3.75×10^{-3}	2.52×10^{-3}	2.06×10^{-3}
$\Delta t_s \nu / u_\tau^2$	0.675	0.539	0.494
$\Delta \omega$	5.2	7.8	9.5
N_s	2560	5120	4160

TABLE 1. Temporal resolution parameters

The first term on the right-hand side of (1) represents the pressure source that results from the linear interaction of the mean shear with the turbulence. The next six terms are the pressure source terms that result from the nonlinear interactions of the turbulent flow field.

The pressure intensity normalized by the mean shear, shown in figure 1, decreases across the layer with increasing curvature. In particular, the near-wall maximum of the pressure intensity is reduced by increasing the curvature. A similar decrease in magnitude occurs in the pressure source terms (figure 2). The intensity, skewness and flatness of the wall pressure fluctuations of the transversely curved flows are compared to their plane channel counterparts in table 2.

Contrary to what was generally accepted (Kraichnan 1956; Panton & Linebarger 1974), Kim (1989) found that in turbulent channel flow the nonlinear turbulence field interactions constitute the strongest sources of pressure fluctuations. The same is true in the current transversely curved flows.

In the plane channel the maximum of the mean square of the nonlinear terms occurs at about $y^+ \approx 20$, which is the same as the mean position of the near-wall vortices as well as the position of the maximum of the pressure intensity (Kim 1989). In the transversely curved flows, the maximum of the pressure intensity is weakened as the curvature increases and it is at about the same position as in the plane channel flow
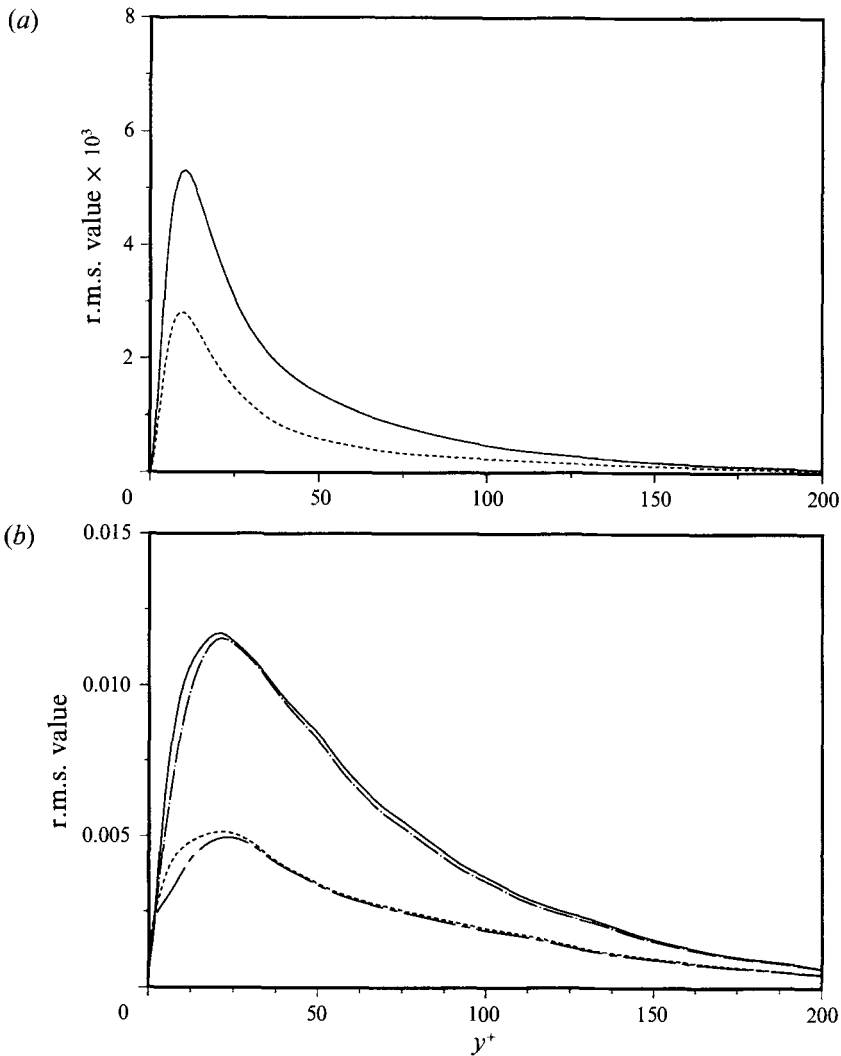
(a)

r.m.s. value $\times 10^3$

(b)

r.m.s. value

y^+

FIGURE 2. Profiles of the root-mean-square value of the pressure source terms normalized by ν and u_τ: (a) linear contribution: cylinders with ———, $\gamma = 5$ and ————, $\gamma = 11$; (b) nonlinear contribution: cylinders with ———, $\gamma = 5$ and ————, $\gamma = 11$; total source terms: cylinders with —·——, $\gamma = 5$ and ————, $\gamma = 11$.

γ	0	5	11
$\overline{p_w^2}^{1/2}$	1.54	0.84	0.58
$S(p_w)$	-0.03	-0.70	-0.78
$F(p_w)$	5.16	7.16	6.18

TABLE 2. Wall pressure parameters

($y^+ \approx 20$, figure 1). Similarly, as the curvature increases, the average strength of the near-wall vortices is weakened while the average position of the vortex cores remains the same ($y^+ \approx 20$) (see §5 of Part 1).

In order to associate the pressure intensity with the sources of pressure fluctuations
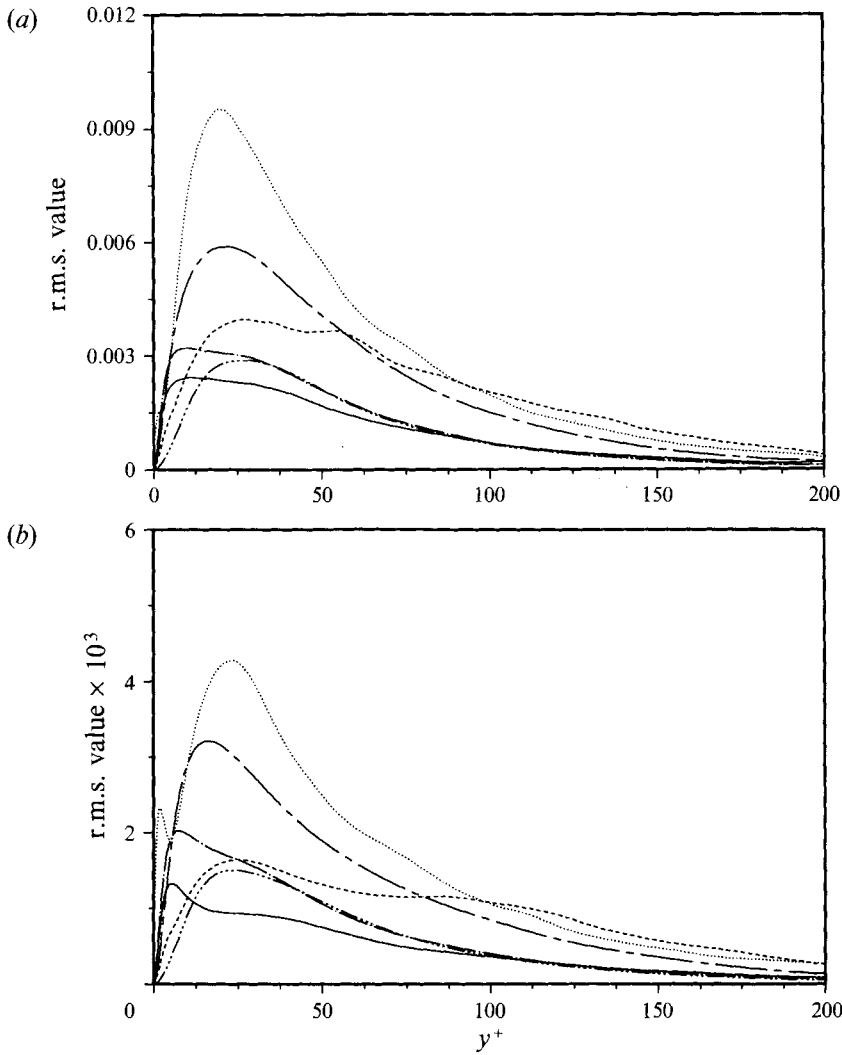
FIGURE 3. Profiles of the root-mean-square value of the nonlinear contributions to the source terms normalized by ν and u_τ: (a) $\gamma = 5$, (b) $\gamma = 11$; —— $(\partial v_r/\partial r)^2$, ... $(2/r)(\partial v_r/\partial \theta - v_\theta)(\partial v_\theta/\partial r)$, —·— $(1/r^2)(\partial v_\theta/\partial \theta + v_r)^2$, —··— $(\partial v_z/\partial z)^2$, ———— $2(\partial v_z/\partial r)(\partial v_r/\partial z)$, ———— $(2/r)(\partial v_z/\partial \theta)(\partial v_\theta/\partial z)$.

in the flow, the various contributions to the nonlinear source terms of the pressure are examined (figure 3). The most important nonlinear pressure source term in the transversely curved flow is

$$\frac{2}{r}\left(\frac{\partial v_r}{\partial \theta} - v_\theta\right)\frac{\partial v_\theta}{\partial r}. \tag{3}$$

This term includes significant contributions from the near-wall streamwise vortices, as does its counterpart in the plane channel. Note also that in both flows this source term develops near-wall ($y^+ \approx 5$) local extrema. Vorticity of opposite sign to the primary vortices in the vicinity of the wall may be responsible for this behaviour.

Figure 3 also shows that, as the curvature increases, another nonlinear term,

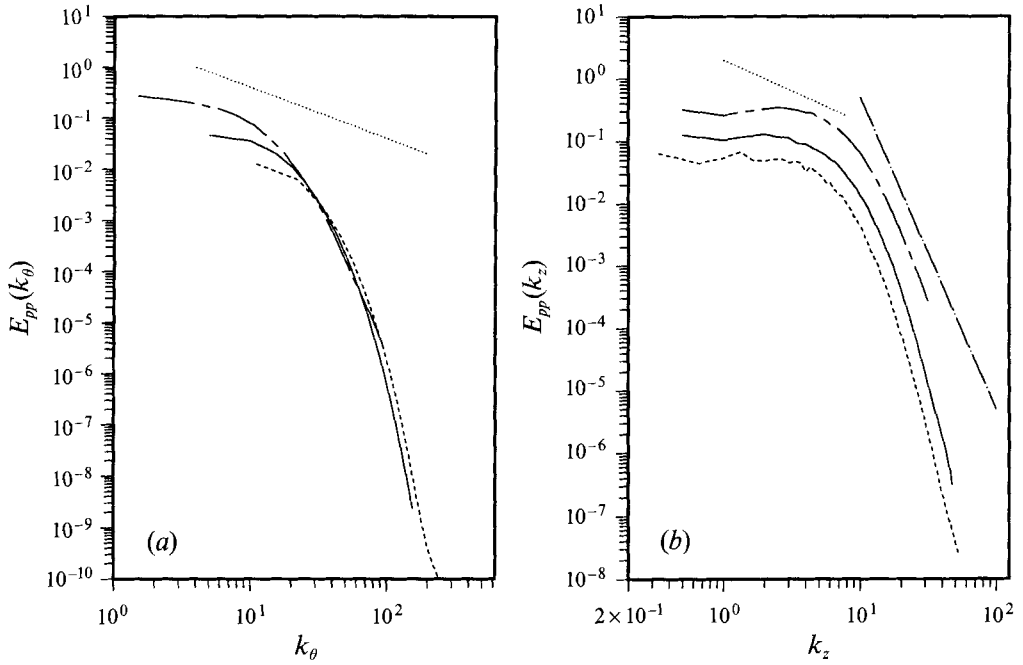$$\frac{2}{r}\frac{\partial v_z}{\partial \theta}\frac{\partial v_\theta}{\partial z}, \tag{4}$$

FIGURE 4. Spectra of the wall pressure fluctuations (*a*) azimuthal (spanwise) spectra, (*b*) axial (streamwise) spectra; ————, plane channel (Choi & Moin 1990); cylinders ($\delta\Delta k_\theta = \gamma$) with ———, $\gamma = 5$ and ————, $\gamma = 11$; ·········, -1 slope; —·—, -5 slope.
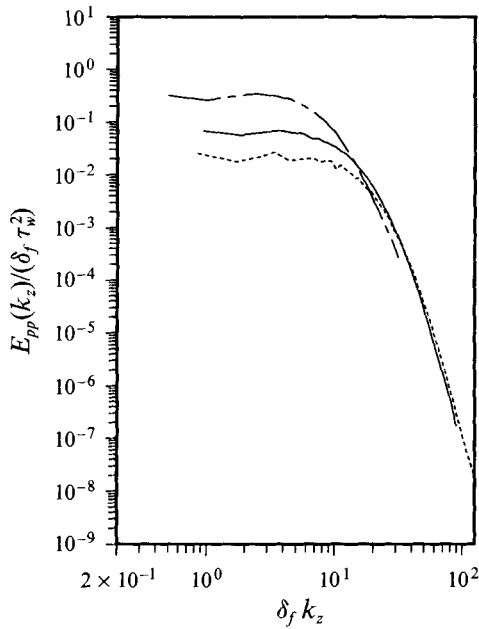
FIGURE 5. Axial (streamwise) spectra of the wall pressure fluctuations normalized by δ_f and u_r: ————, plane channel (Choi & Moin 1990) ($\gamma = 0, \delta_f = \delta$); cylinders with ———, $\gamma = 5$ and ————, $\gamma = 11$.
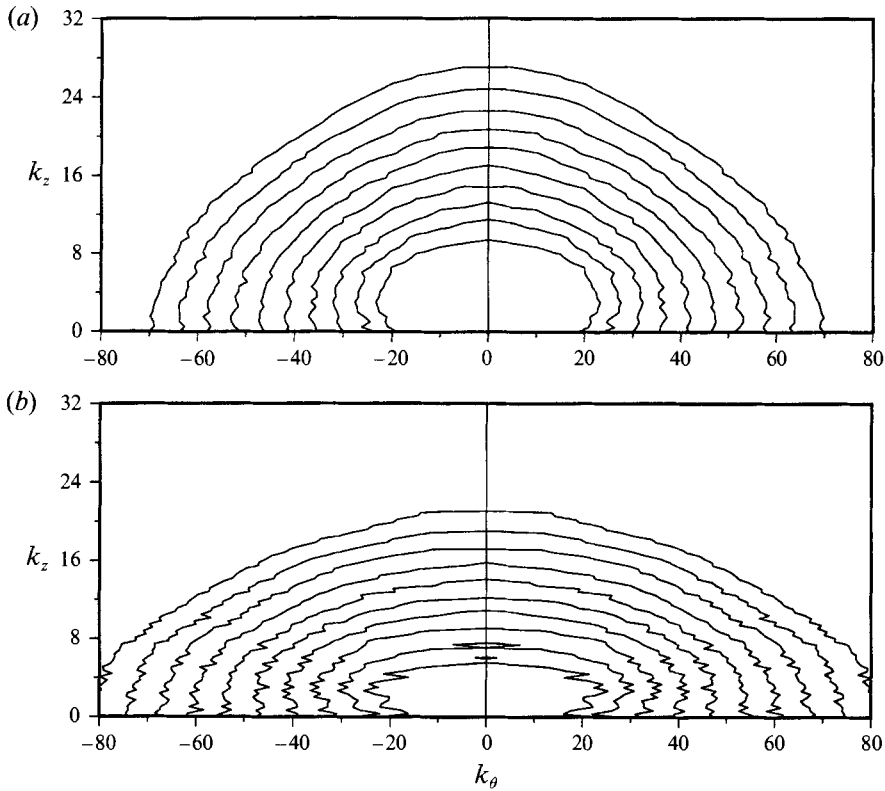
FIGURE 6. Spectra of the wall pressure fluctuations ($\delta\Delta k_\theta = \gamma$, and the scale of the ordinate is twice that of the abscissa): (a) $\gamma = 5$, (b) $\gamma = 11$. The contour levels are logarithmically distributed from 10^{-6} to 10^{-3} with exponent increments of 0.3.

plays an increasingly important role in the pressure fluctuations. Note that the factors in this product are the two velocity gradients that define the radial component of the vorticity. As the curvature increases, strong normal vorticity fluctuations (relative to the local streamwise vorticity fluctuations) become increasingly more common farther away from the wall (see figures 17 and 18 of Part 1).

3. Spatial spectra

The one-dimensional wall pressure spectra as a function of the azimuthal (spanwise) and axial (streamwise) wavenumbers are shown in figure 4, along with their planar counterparts (Choi & Moin 1990). Note that the spanwise spectra (figure 4a) is not affected by the transverse curvature in the high wavenumber range. In the low wavenumber range the intensity of the spanwise spectra decreases with increasing curvature. This suggests that the curvature mostly affects structures with large spanwise lengthscales (small k_θ). The streamwise spectral density of the wall pressure fluctuations decreases significantly with curvature for all scales (figure 4b). The three flows display a negligible wavenumber range with the -1 slope in the streamwise spectrum, owing to the low Reynolds numbers. The high wavenumber range of the streamwise spectrum has a -5 (see Blake 1986) slope in the planar case. In the transversely curved flows the axial spectra exhibit steeper slopes in the high
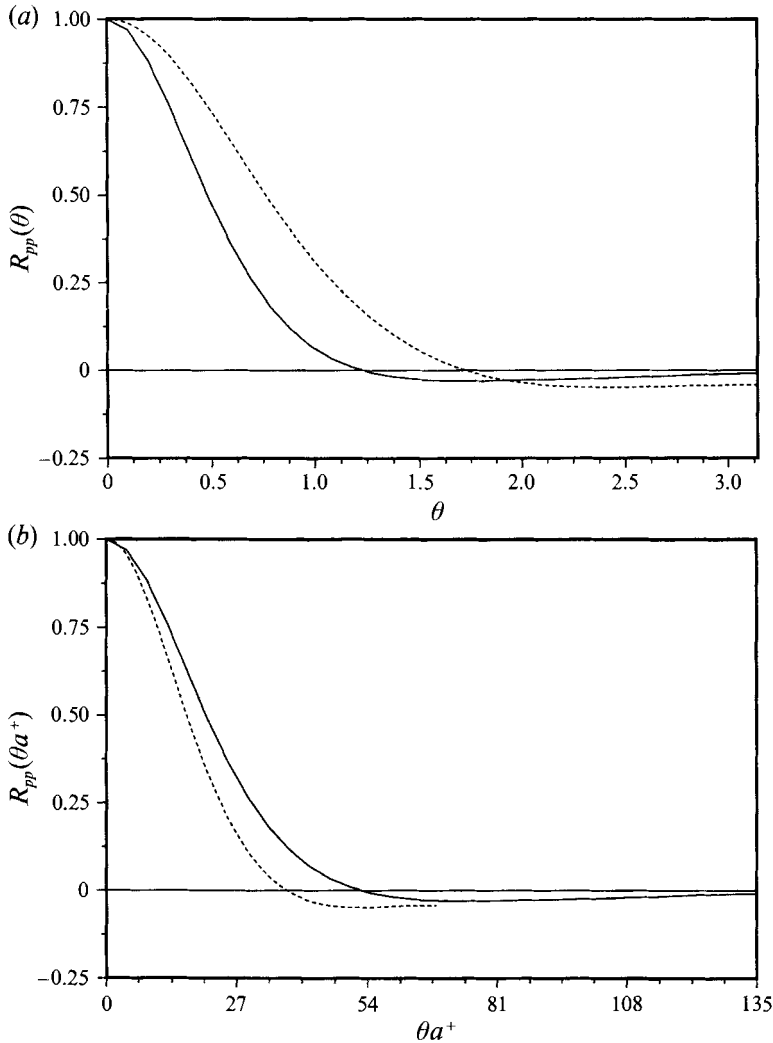
FIGURE 7. Azimuthal (spanwise) two-point correlations of the wall pressure fluctuations as a function of (a) θ (radians) and (b) θa^{+}: ———, $\gamma = 5$ ($a^{+} \approx 43$); –––––, $\gamma \approx 11$ ($a^{+} \approx 21$).

wavenumber range, indicating a weakening of structures in the buffer layer that contribute to the wall pressure fluctuations.

In a transversely curved boundary layer, the volume of turbulent flow that must be supported per unit wall surface area is larger than in the plane channel case by a factor of $1 + \frac{1}{2}\gamma$. This is a natural curvature parameter. It was found that when scaled with the curvature dependent lengthscale given by

$$\delta_f = \delta(1 + \tfrac{1}{2}\gamma)^{1/2}, \tag{5}$$

the axial (streamwise) spectrum of the wall pressure fluctuations of the plane channel flow and of the transversely curved flows collapse in the high wavenumber range, as shown in figure 5. This lengthscale is related to the velocity scale defined in §3.3 of Part 1 (see §6).

The two-dimensional spatial wall pressure spectra are shown in figure 6. As in the planar case (see figure 12 of Choi & Moin 1990) the transversely curved spectra are
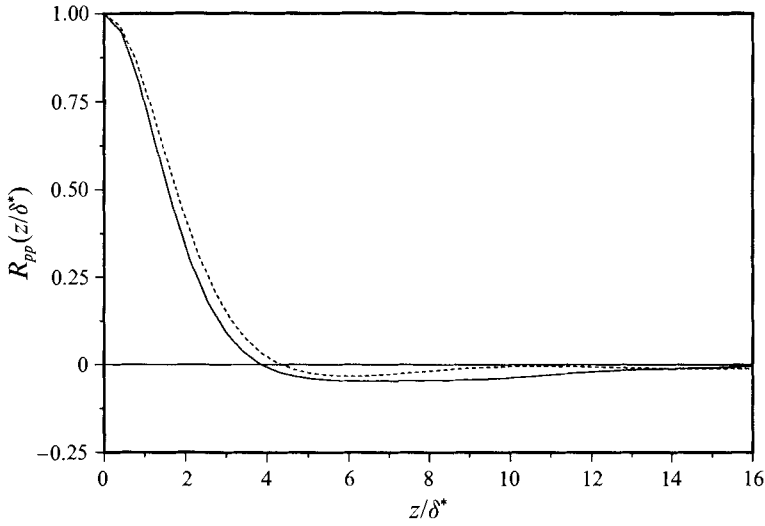
FIGURE 8. Axial (streamwise) two-point correlations of the wall pressure fluctuations:
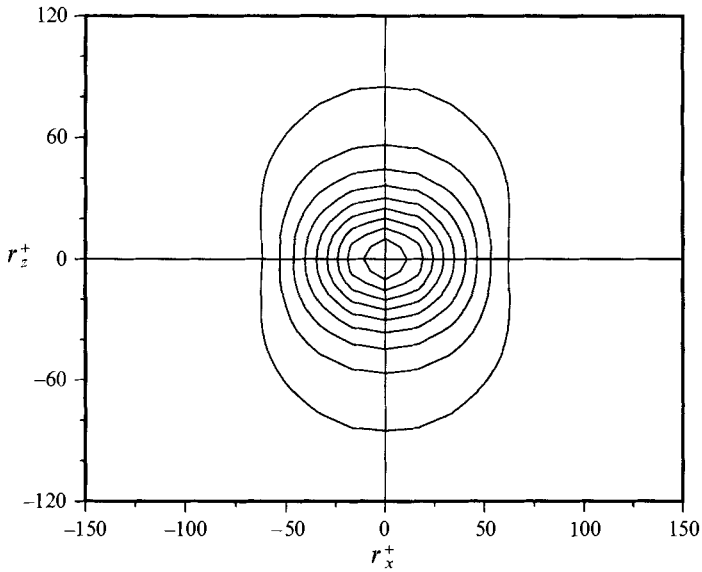——, $\gamma = 5$ and ----, $\gamma = 11$.

FIGURE 9. Contour plot of two-point correlations of the wall pressure fluctuations for plane channel (Choi & Moin 1990) as a function of the streamwise (r_x^+) and spanwise (r_z^+) separations. The contour levels are from 0.1 to 0.9 with increments of 0.1.

elongated in the spanwise direction. However, as the curvature increases the azimuthal (spanwise) elongation of the spectrum increases. In addition the energy of the large structures (small k_z or k_θ) decreases with increasing curvature.

4. Two-point correlations

In two previous studies of the wall pressure fluctuations in boundary layers with transverse curvature (Willmarth & Yang 1970; Willmarth et al. 1976) it was shown
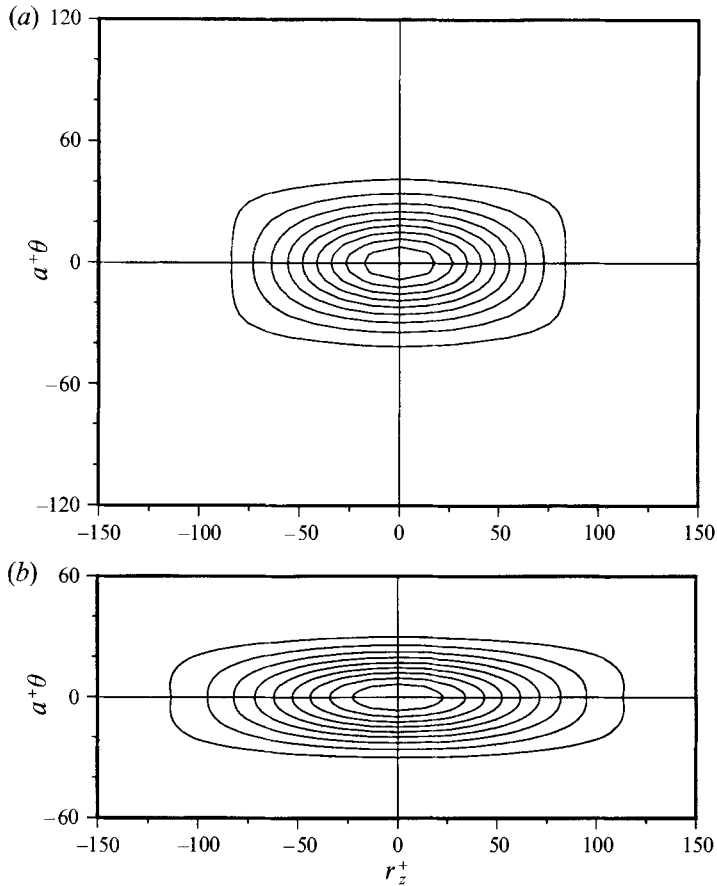
FIGURE 10. Contour plot of two-point correlations of the wall pressure fluctuations for (*a*) $\gamma = 5$ and for (*b*) $\gamma = 11$ as a function of the axial (r_z^+-streamwise) and azimuthal ($a^+\theta$-spanwise) separations. The contour levels are from 0.1 to 0.9 with increments of 0.1.

that, as the curvature increases, the wall pressure becomes better correlated around the cylinder. This trend is also evident in the present flows as shown in figure 7(*a*). Note, however, that in viscous units the azimuthal (spanwise) correlation length decreases with increasing curvature (figure 7*b*). In the axial two-point correlations (figure 8), the zero-crossing point (i.e. where $R_{pp}(z/\delta^*) = 0$) is at $z/\delta^* = 3.4$, 3.9 and 4.6 for the plane channel, the $\gamma = 5$ and the $\gamma = 11$ flows, respectively. These values show a distinct increase with curvature and are higher than the value of 2 reported by Willmarth & Yang (1970) and Willmarth *et al.* (1976).

For small separations, the wall pressure correlation contours in the planar case (Willmarth & Wooldridge 1962; Choi & Moin 1990) are nearly circular and, as the separation increases, the ratio of the spanwise to the streamwise lengthscales increases. In contrast, in a transversely curved flow Willmarth & Yang (1970) ($\gamma = 2$ and $a^+ \approx 4500$) report wall pressure correlation contours which, for large separations, are compressed in the spanwise direction. However, the $\gamma = 4$ measurements of Willmarth *et al.* (1976) seem to be inconsistent with this trend, in that their correlation contours are elongated in the spanwise direction (as in the planar flow) even though the curvature is stronger than in Willmarth & Yang (1970). Figure 9 shows the correlation contours of the wall pressure fluctuations for the plane channel flow. In contrast, figure
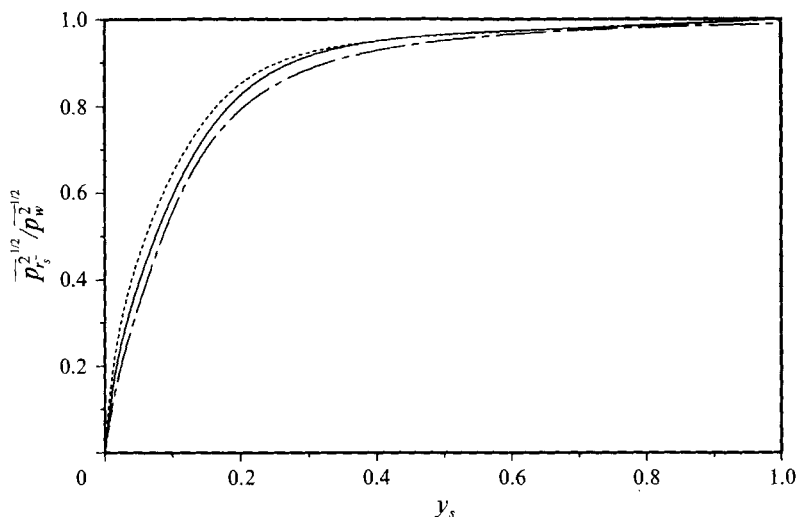
FIGURE 11. Fractional contributions to the root-mean-square wall pressure fluctuations from sources located at $y_0 \in [0, y_s]$: ————, plane channel; cylinders with ———, $\gamma = 5$ and ————, $\gamma = 11$ ($y_s = r_s - a$). The result is normalized by the total wall pressure intensity.

10 shows that as the curvature increases, there is a significant increase in the ratio of the axial (streamwise) to azimuthal (spanwise) lengthscales for all separations.

5. Green function representation

Further insight into the spatial structure of the wall pressure fluctuations can be obtained by representing the pressure field in terms of the Green function of the Poisson operator.

In transversely curved flows the Fourier coefficient of the wall pressure fluctuations is given by (Neves *et al.* 1992)

$$\hat{p}(r) = \int_a^{a+1} \mathcal{G}(r, r_0) \hat{f}(r_0) \, r_0 \, dr_0 + a \mathcal{G}(r, a) \frac{d\hat{p}}{dr}\bigg|_{r=a} - (a+1) \mathcal{G}(r, a+1) \frac{d\hat{p}}{dr}\bigg|_{r=a+1}, \qquad (6)$$

where r_0 is the radial position of the source, $\hat{f}$ denotes the Fourier transform of the source of the pressure Poisson equation (equation (1)) and $\mathcal{G}$ is the Green function of the Laplacian operator in cylindrical coordinates with derivative boundary conditions. From (6) the Fourier coefficients of the contributions to the wall pressure fluctuations ($\hat{p}_{r_s^-}$) from sources located in the volume close to the cylinder surface at $a \leqslant r_0 \leqslant r_s$ are given by

$$\hat{p}_{r_s^-} = \int_a^{r_s} \mathcal{G}(a, r_0) \hat{f}(r_0) \, r_0 \, dr_0 + a \mathcal{G}(a, a) \frac{d\hat{p}}{dr}\bigg|_{r=a} - r_s \mathcal{G}(a, r_s) \frac{d\hat{p}}{dr}\bigg|_{r=r_s}. \qquad (7)$$

Likewise, the Fourier coefficients of the contributions of the outer part of the flow volume ($r_s \leqslant r_0 \leqslant a+1$) to the wall pressure fluctuations ($\hat{p}_{r_s^+}$) are given by

$$\hat{p}_{r_s^+} = \int_{r_s}^{a+1} \mathcal{G}(a, r_0) \hat{f}(r_0) \, r_0 \, dr_0 + r_s \mathcal{G}(a, r_s) \frac{d\hat{p}}{dr}\bigg|_{r=r_s} - (a+1) \mathcal{G}(a, a+1) \frac{d\hat{p}}{dr}\bigg|_{r=a+1}. \qquad (8)$$

Similar expressions can be obtained for the plane channel. The root-mean-square of the contributions to the wall pressure fluctuations normalized by the total wall r.m.s. pressure is shown in figure 11 as a function of the cutoff r_s. For the two transversely
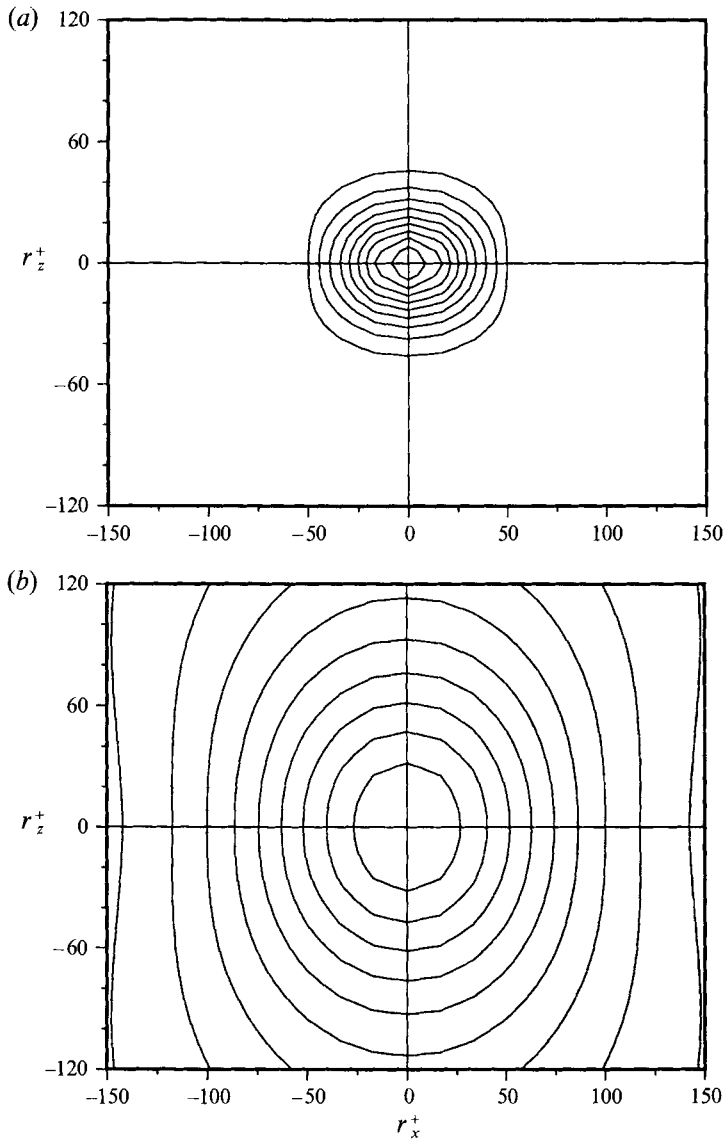
FIGURE 12. Contour plot of two-point correlations of the contributions to the wall pressure fluctuations in the plane channel from flow in the interval (a) $[0, y_s]$ and (b) $[y_s, 1]$ (1 denotes the channel centreline) as a function of the streamwise (r_x^+) and spanwise (r_z^+) separations. The contour levels are from 0.1 to 0.9 with increments of 0.1 and $y_s = 0.19$ ($y_s^+ = 35.4$).

curved flows and the plane channel, more than 80% of the wall r.m.s. pressure fluctuations are produced by the inner part of the domain ($y_s = r_s - a \approx 0.2$). Note that, as the curvature increases, there is a slight increase in the wall pressure fractional contributions from the near-wall ($y_s < 0.2$) part of the flow.

Small separation correlation contours result from small-scale pressure fluctuations typically associated with the inner part of the boundary layer, while the large separation correlation contours have significant contributions from large-scale motions in the outer part of the boundary layer. This is demonstrated in figure 12 which shows the plane channel two-point correlations of $p_{y_s^-}$ and $p_{y_s^+}$ for $y_s \approx 0.2$. It is clear that the
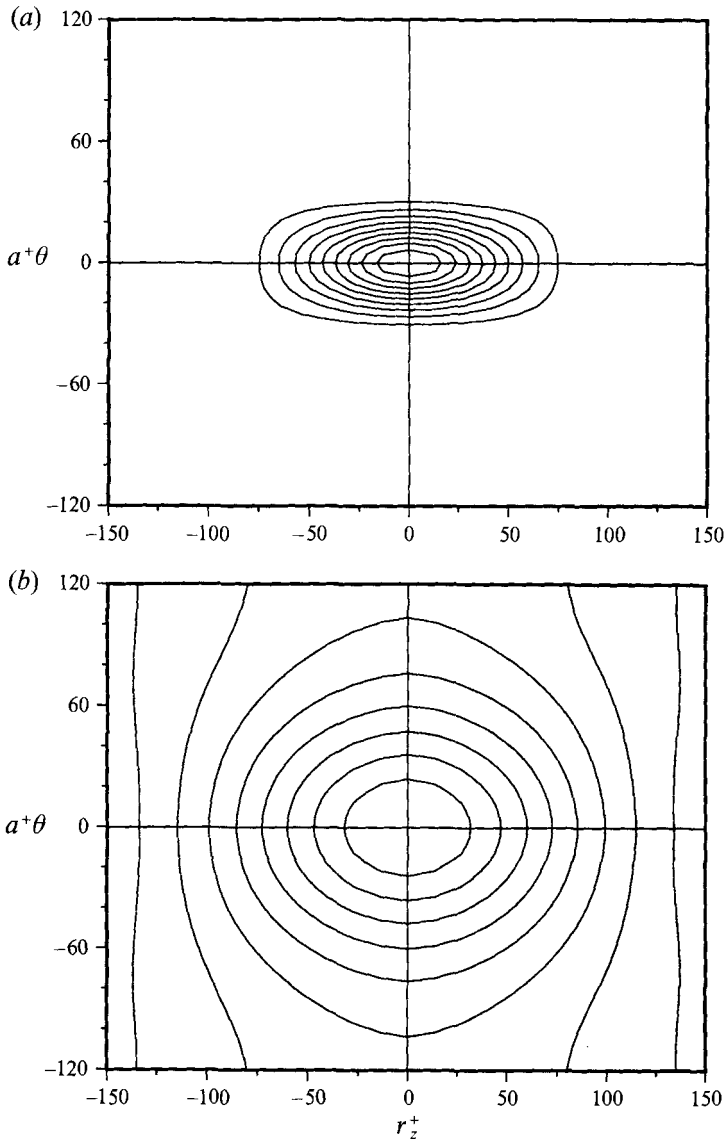
FIGURE 13. Contour plot of two-point correlations of the contributions to the wall pressure fluctuations for $\gamma = 5$ from flow in the interval (a) $[a, r_s]$ and (b) $[r_s, a+1]$ as a function of the axial (r_z^+-streamwise) and azimuthal ($a^+\theta$-spanwise) separations. The contour levels are from 0.1 to 0.9 with increments of 0.1 and $y_s = 0.2$ ($y_s^+ = 43.8$).

spanwise elongation of the planar wall pressure correlation contours is due to disturbances in the outer part of the layer (figure 12b). Note also that for this cutoff ($y_s \approx 0.2$) the shape of the planar wall pressure correlation contours due to the inner part of the flow are slightly elongated in the streamwise direction (figure 12a).

The two-point correlations of $p_{r_s^-}$ and $p_{r_s^+}$ for $y_s = r_s - a \approx 0.2$ are shown in figures 13 and 14 for $\gamma = 5$ and for $\gamma = 11$, respectively. In both cases the two-point correlations of the wall pressure fluctuations due to contributions from the volume close to the cylinder have a streamwise aspect ratio similar to that shown in figure 10 for the contributions of the whole flow. On the other hand, in the $\gamma = 5$ flow, the shape
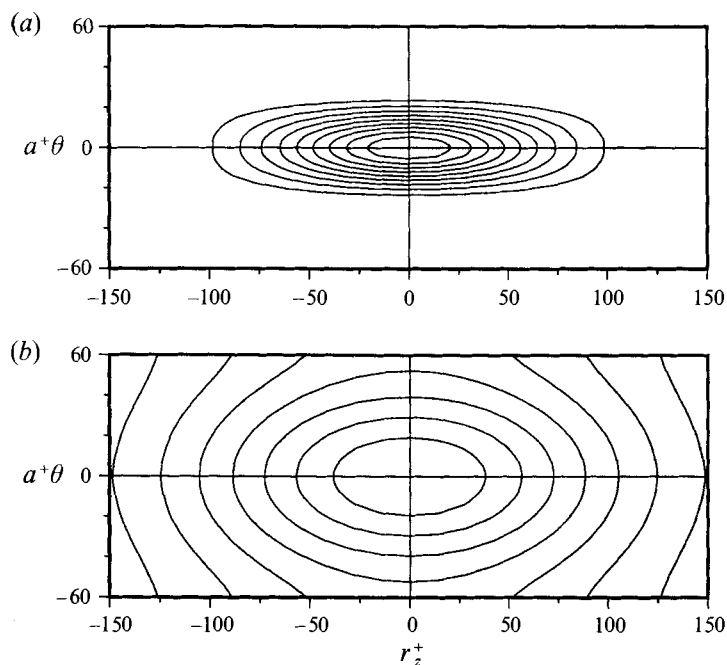
FIGURE 14. Contour plot of two-point correlations of the contributions to the wall pressure fluctuations for $\gamma = 11$ from flow in the interval (a) $[a, r_s]$ and (b) $[r_s, a+1]$ as a function of the axial (r_z^+-streamwise) and azimuthal ($a^+\theta$-spanwise) separations. The contour levels are from 0.1 to 0.9 with increments of 0.1 and $y_s = 0.2$ ($y_s^+ = 47.7$).

of the correlation contours of the wall pressure fluctuations due to the outer part of the flow (figure 13b) have a spanwise orientation for large separations. As the curvature increases there is an increase in the streamwise orientation of the contours of the outer contribution (see figures 12b, 13b and 14b). Wall pressure correlation contours due to the outer part of the flow, obtained for larger values of the cutoff ($y_s > 0.2$, not shown), become increasingly oriented in the spanwise direction in both transversely curved flows ($\gamma = 5$ and $\gamma = 11$) and the spanwise stretching effect of the outer part of the flow on the wall pressure correlations decreases as the curvature increases.

The wall pressure correlations due to the near-wall part of the flow are elongated in the streamwise direction, suggesting that the near-wall structures are responsible for this shape. The curvature trend shown in figures 12–14 is consistent with the lengthscale parameter L^* based on the streamwise velocity fluctuations v_z (see §6, (18) and figure 24 of Part 1) which suggests that relative to the plane channel, as the curvature increases, the ratio of the streamwise to spanwise lengthscales increases near the wall for both flows and away from the wall in only the $\gamma = 11$ case.

6. Temporal spectra

Figure 15 shows a sample of the time traces of the wall pressure fluctuations normalized by their r.m.s. values. Note that, as the curvature increases, the high-frequency content of the fluctuations is weakened. Apparently the different appearances of the wall pressure fluctuations in the two transversely curved flows, does not noticeably affect the flatness and skewness values (see table 2).
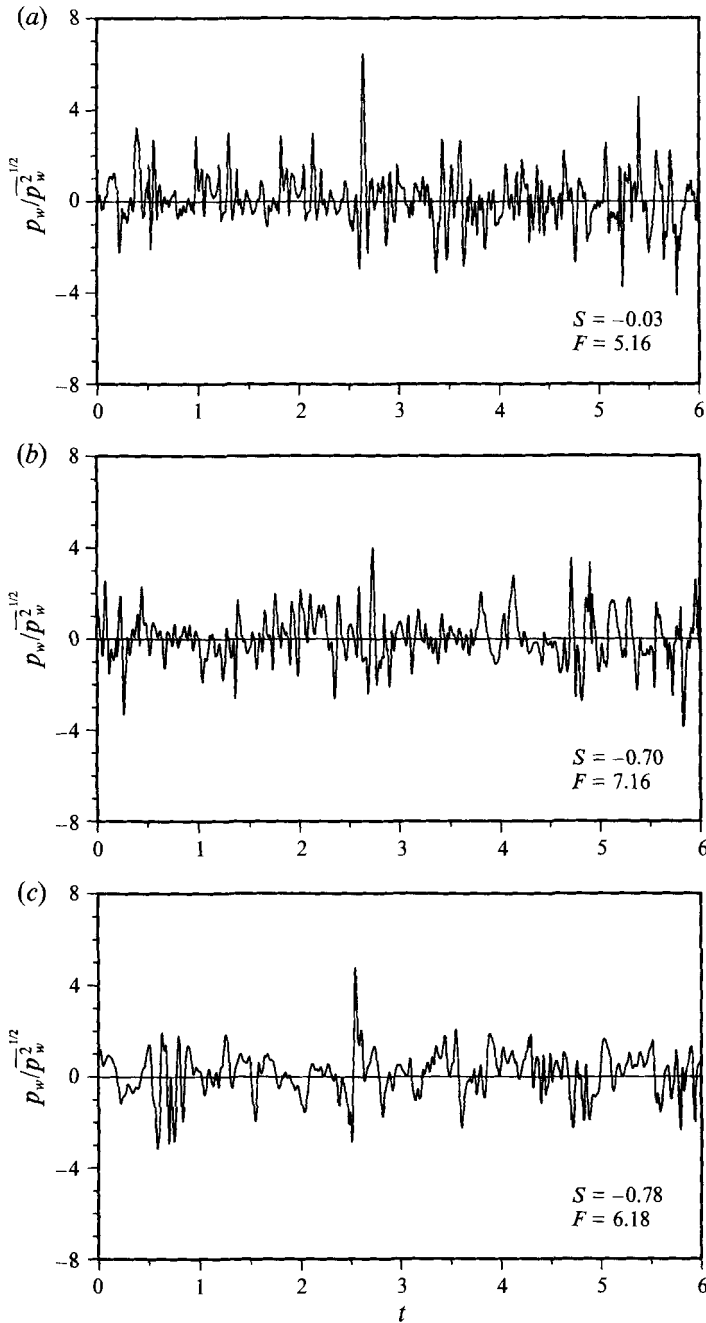
FIGURE 15. Signal of the wall pressure fluctuations normalized by $\overline{p_w^2}^{1/2}$: (*a*) plane channel; cylinders with (*b*) $\gamma = 5$; (*c*) $\gamma = 11$.

The temporal spectra of the wall pressure fluctuations of the two transversely curved turbulent flows are compared to their planar counterpart in figure 16(*a*). As expected from the streamwise one-dimensional spectra, the temporal spectra decrease at all frequencies with increasing curvature.

In the wall pressure temporal spectra measurements of Willmarth & Yang (1970)
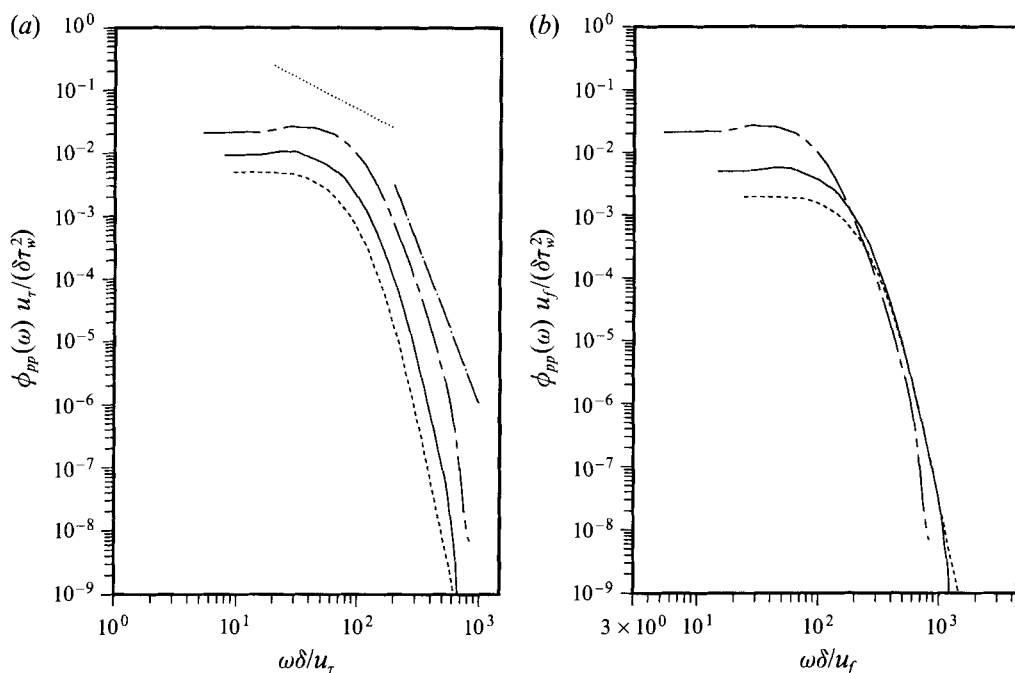
FIGURE 16. Temporal spectra of the wall pressure fluctuations normalized by τ_w^2: (a) δ/u_τ timescale; (b) δ/u_f timescale. ———, plane channel (Choi & Moin 1990) ($\gamma = 0, u_f = u_\tau$); cylinders with ———, $\gamma = 5$ and ----, $\gamma = 11$; ········, -1 slope; —·—, -5 slope.

and Willmarth *et al.* (1976), a reduction in the intensity of the high-frequency range was also observed. However, because of large a^+ the effect of curvature on the inner part of the boundary layer, and therefore on the high-frequency range of their wall pressure temporal spectra should have been negligible.

Using the curvature dependent lengthscale defined in §3 (equation (5)), a curvature dependent timescale (δ_f/u_τ) can be defined:

$$\frac{\delta_f}{u_\tau} = \frac{\delta}{u_\tau}(1 + \tfrac{1}{2}\gamma)^{1/2}. \tag{9}$$

When scaled with this curvature-dependent timescale the temporal spectra of the wall pressure fluctuations of the two transversely curved flows collapse with their planar counterpart in the high-frequency range (figure 16b). Also note that this timescale is related to the velocity scale $\tilde{u}$ defined in Part 1 (see Part 1, §4.3) by

$$\frac{\delta_f}{u_\tau} = \frac{\delta}{\tilde{u}(y = 1)}. \tag{10}$$

7. Convection velocity and Taylor's hypothesis

The notion that structures in the flow are convected at a velocity close to the free-stream velocity has received substantial experimental support in planar boundary-layer flows. Experimentally, it is easier to measure temporal spectra, from which streamwise spectra are obtained by invoking Taylor's hypothesis.
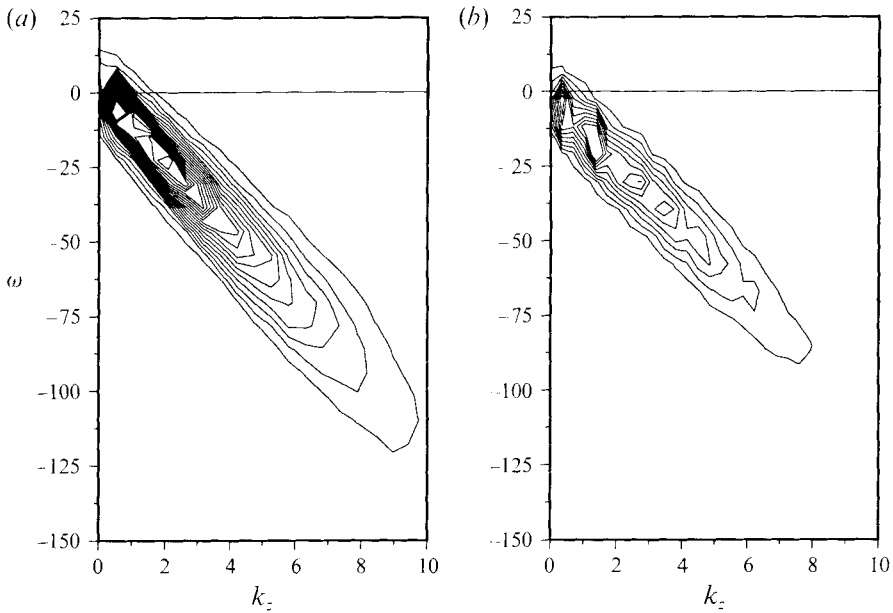
FIGURE 17. Contour plot of the axial (streamwise) wave-number-frequency spectra of the wall pressure fluctuations: (a) $\gamma = 5$ and the contour levels are from 0.000 35 to 0.0070; (b) $\gamma = 11$ and the contour levels are from 0.000 35 to 0.0035. The contour increments are 0.000 35.
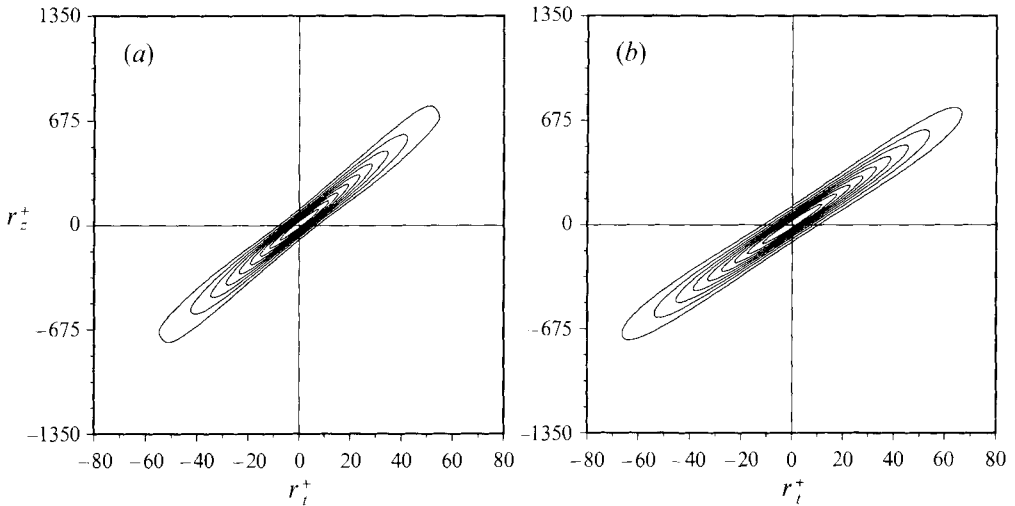

FIGURE 18. Contour plot of two-point correlations of the wall pressure fluctuations as a function of the axial (streamwise) spatial (r_z^+) and temporal (r_t^+) separations: (a) $\gamma = 5$; (b) $\gamma = 11$. The contours are from 0.1 to 0.9 with increments of 0.1.

The frequency/axial (streamwise) wavenumber power spectra, $\Phi_{pp}(k_z, \omega)$, for the two transversely curved flows are shown in figure 17. As has been the case throughout this study the intensity decreases as the curvature increases for all frequencies and axial lengthscales. In both cases the narrow aspect ratios of the iso-contours denote well-defined convection velocities.
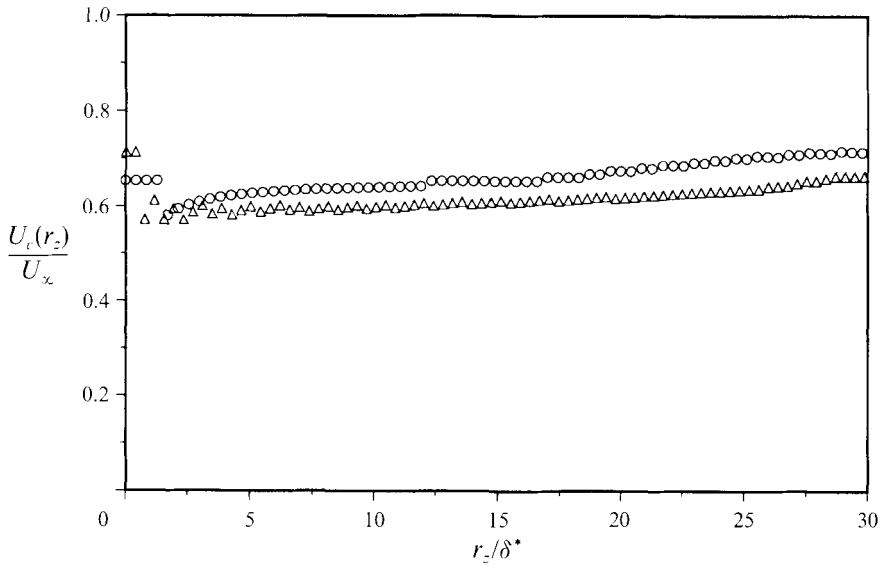
FIGURE 19. Convection velocity normalized by U_x as a function of the axial (streamwise) separation (r_z/δ^*); $\bigcirc$, for $\gamma = 5$ and $\triangle$, for $\gamma = 11$.

The space–time correlation of the wall pressure fluctuations is given by the Fourier transform of the frequency/streamwise wavenumber spectrum,

$$R_{pp}(r_z, r_t) = \sum_{k_z} \sum_{\omega} \Phi_{pp}(k_z, \omega) \exp(-i\omega r_t) \exp(-ik_z r_z), \tag{11}$$

and is shown in figure 18 for the two transversely curved flows. When measured in viscous units, the axial lengthscales of the auto-correlation contours are virtually unaffected by curvature, however, the temporal scale increases with curvature, since the convection velocities are different (see below). Again, clearly defined convection velocities are evident from the oblong shape of the contours.

Several definitions for the convection velocity have been proposed in the literature (Wills 1964). The most common are obtained from the frequency/streamwise wavenumber spectrum, $\Phi_{pp}(k_z, \omega)$, or from its Fourier transform, $R_{pp}(r_z, r_t)$.

For example, the convection velocity as a function of the axial (streamwise) separation (r_z) for a given time delay (r_{t_c}), is defined as the ratio r_z/r_{t_c} for which $R_{pp}(r_z, r_{t_c})$ is a maximum,

$$U_c(r_z) = \frac{r_z}{r_{t_c}}, \quad \left.\frac{\partial R_{pp}}{\partial r_z}(r_z, r_t)\right|_{r_t = r_{t_c}} = 0. \tag{12}$$

Likewise, the convection velocity can be defined as a function of the temporal separation (r_t) according to

$$U_c(r_t) = \frac{r_{z_c}}{r_t}, \quad \left.\frac{\partial R_{pp}}{\partial r_t}(r_z, r_t)\right|_{r_z = r_{z_c}} = 0. \tag{13}$$

The convection velocities of the wall pressure fluctuations computed from (12) and (13) are shown in figures 19 and 20, respectively. These convection velocities are lower than in the plane channel. As the axial separation increases, the convection velocity
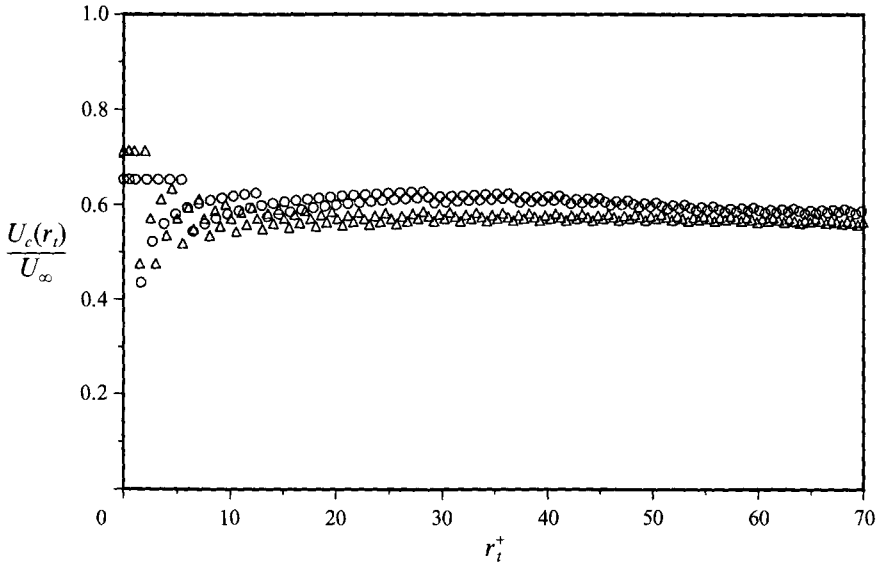
FIGURE 20. Convection velocity normalized by U_∞ as a function of the temporal separation (r_t^+); $\bigcirc$, for $\gamma = 5$ and $\triangle$, for $\gamma = 11$.
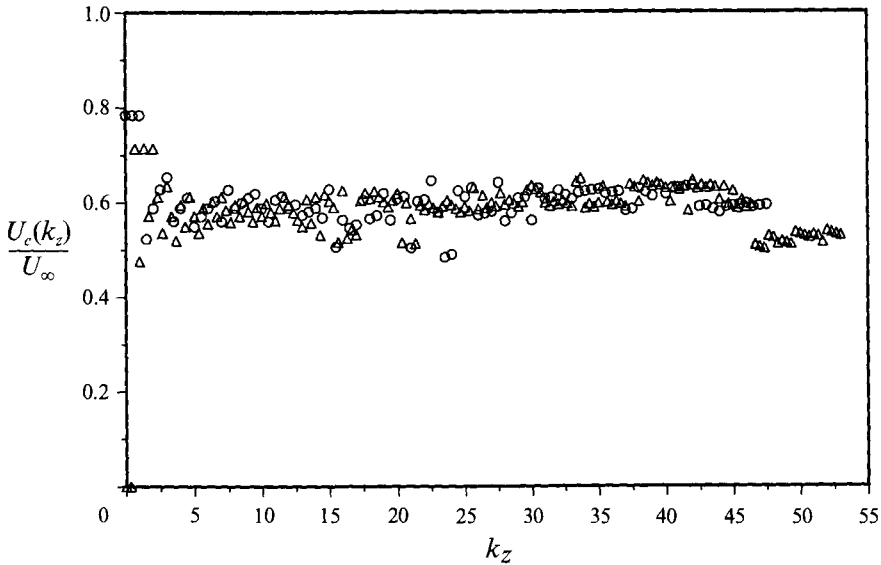

FIGURE 21. Convection velocity normalized by U_∞ as a function of the streamwise wave number: $\bigcirc$, for $\gamma = 5$ and $\triangle$, for $\gamma = 11$.

increases to about $0.7U_\infty$ for $\gamma = 5$ and to about $0.65U_\infty$ for $\gamma = 11$. Note, however, that as a function of the temporal separation the convection velocity is practically constant in both flows $(U_c \simeq 0.6U_\infty)$.

The convection velocity can also be defined as a function of the streamwise wavenumber (Wills 1970),

$$U_c(k_z) = -\frac{\omega_c}{k_z}, \quad \frac{\partial \Phi_{pp}}{\partial \omega}(k_z, \omega)\bigg|_{\omega = \omega_c} = 0, \tag{14}$$
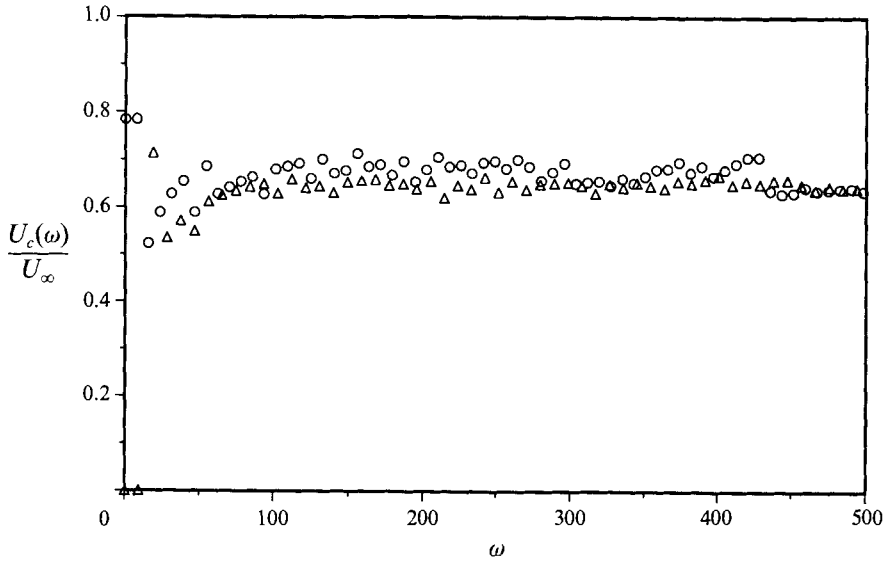
FIGURE 22. Convection velocity normalized by U_∞ as a function of frequency: cylinders: $\bigcirc$, for $\gamma = 5$ and $\triangle$, for $\gamma = 11$.

and as a function of the frequency,

$$U_c(\omega) = -\frac{\omega}{k_{z_c}}, \quad \frac{\partial \Phi_{pp}}{\partial k_z}(k_z, \omega)\bigg|_{k_z = k_{z_c}} = 0. \tag{15}$$

When expressed as a function of the axial wavenumber (figure 21) the convection velocity is about $0.6U_\infty$ for large wavenumbers in all three flows. Likewise, as a function of frequency the convection velocity (figure 22) is about $0.65U_\infty$ in the curved flows, which is lower than the value of about $0.8U_\infty$ for the plane channel (Choi & Moin 1990).

In the cylinder flows, the various convection velocities show little variation among themselves. In the following a constant value of the convection velocity, $0.65U_\infty$, is used to relate the temporal spectrum ($\phi_{pp}(\omega)$) to the axial spectrum ($E_{pp}(k_z)$) according to Taylor's hypothesis:

$$E_{pp_c}(k_{z_c}) = \frac{\phi_{pp}(\omega)}{U_c}, \quad k_{z_c} = \frac{\omega}{U_c}. \tag{16}$$

Comparison of $\phi_{pp}(\omega)$ with $E_{pp_c}(k_{z_c})$ (figure 23) shows that Taylor's hypothesis is a better assumption for low frequencies, as was also observed in the planar case (Choi & Moin 1990).

The decomposition of the two-dimensional spectra $\Phi_{pp}(k_z, \omega)$ and $\Phi_{pp}(k_\theta, \omega)$ into their streamwise and spanwise similarity functions $F_z(k_z U_c/\omega)$ and $F_\theta(k_\theta U_c/\omega)$, are given by

$$\left.\begin{aligned} \Phi_{pp}(k_z, \omega) &= \phi_{pp}(\omega)\frac{U_c(\omega)}{\omega}F_z(k_z U_c/\omega), \\ \Phi_{pp}(k_\theta, \omega) &= \phi_{pp}(\omega)\frac{U_c(\omega)}{\omega}F_\theta(k_\theta U_c/\omega), \end{aligned}\right\} \tag{17}$$

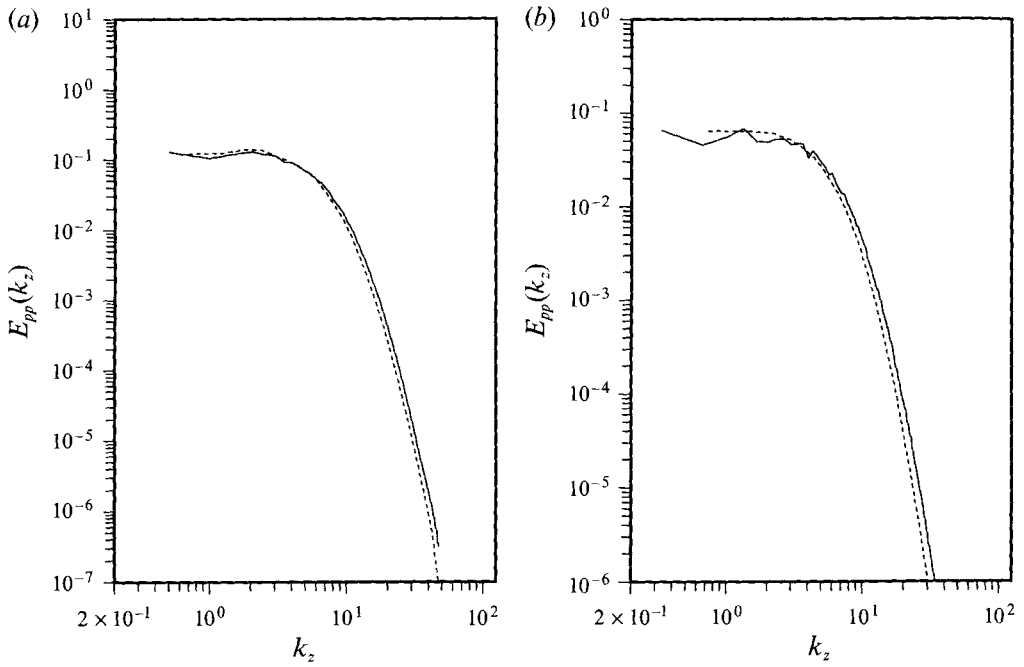respectively (Corcos 1964). Unlike the plane channel where a self-similar behaviour in

FIGURE 23. Conversion of the temporal spectrum to the axial (streamwise) wavenumber spectrum using Taylor's hypothesis for (a) $\gamma = 5$, and for (b) $\gamma = 11$: ———, $E_{pp}(k_z)$; –––––, from $\phi_{pp}(\omega)$ using Taylor's hypothesis ($U_c \simeq 0.65 U_\infty$).
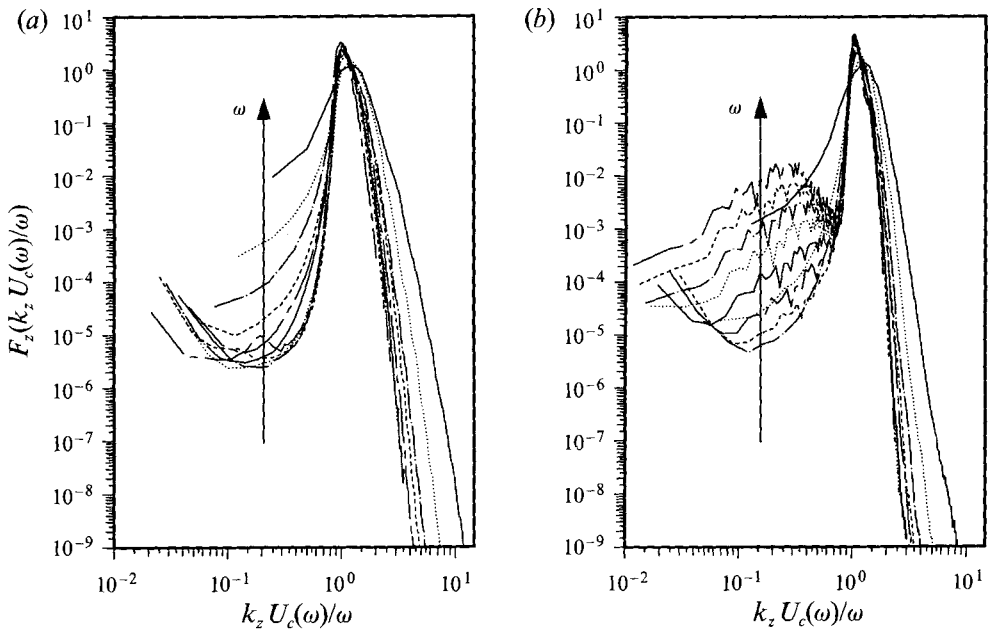

FIGURE 24. Axial (streamwise) similarity function $F_z(k_z U_c(\omega)/\omega)$. The frequency range of ω is: (a) from 31.13 to 311.3 with increments of 31.13 for $\gamma = 5$ and (b) from 38.08 to 380.8 with increments of 38.08 for $\gamma = 11$.

FIGURE 25. Azimuthal (spanwise) similarity function $F_\theta(k_\theta U_c(\omega)/\omega)$. The frequency range of ω is: (a) from 31.13 to 311.3 with increments of 31.13 for $\gamma = 5$ and (b) from 38.08 to 380.8 with increments of 38.08 for $\gamma = 11$.
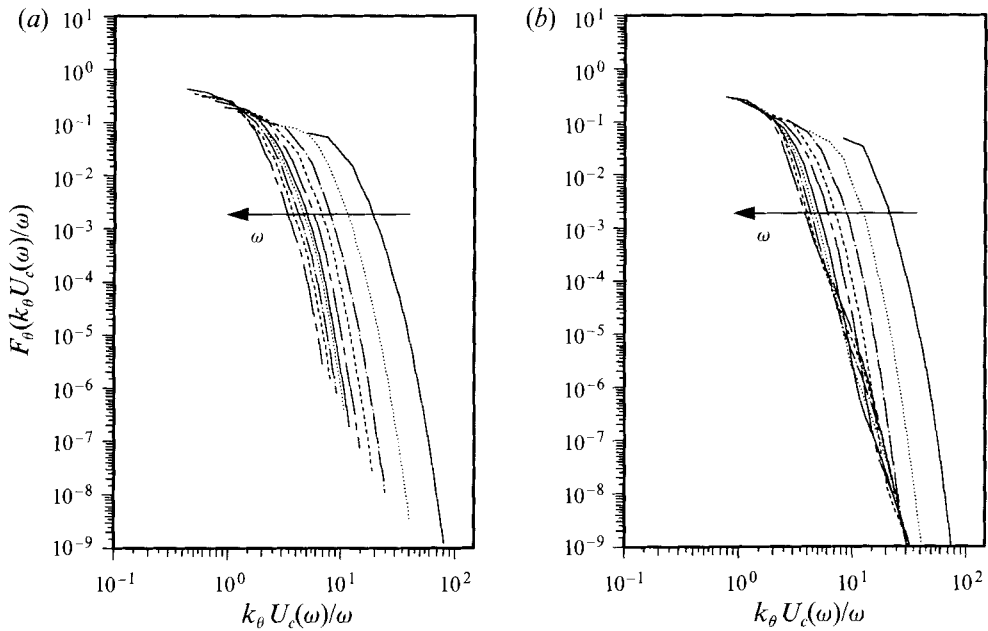
the spanwise direction was observed, no self-similar behaviour is apparent in either $F_z(k_z U_c/\omega)$ or $F_\theta(k_\theta U_c/\omega)$, as shown in figures 24 and 25.

8. Summary and conclusions

The magnitudes of the linear and nonlinear sources of pressure fluctuations are reduced as the curvature increases. The sources associated with streamwise vortices are the strongest, as in planar flows. However, as the curvature increases, a second source of pressure fluctuations associated with the strong wall normal vorticity fluctuations becomes increasingly important.

As the curvature increases, the axial (streamwise) wall pressure spectrum decreases for all scales, whereas the azimuthal (spanwise) wall pressure spectrum decreases only for small wavenumbers (large scales). A curvature-dependent outer lengthscale, which increases with curvature, is proposed from geometrical arguments. This lengthscale collapses the streamwise spectra of the wall pressure fluctuations of the two transversely curved flows with that of the plane channel in the high wavenumber range.

Even though the wall pressure fluctuations become increasingly better correlated around the cylinder, the azimuthal correlation length, when measured in wall units, decreases as the curvature increases. On the other hand, the axial (streamwise) correlation length increases with curvature. Unlike in the planar case, the wall pressure iso-correlation contours are elongated in the streamwise direction, for both large and small separations. Since the streamwise elongation of turbulence structures with curvature is most pronounced near the wall, it is conjectured that the near wall fluctuations are more important in determining the lengthscales of the wall pressure fluctuations. Fractional contributions of the flow (from inner and outer layers) to the wall pressure intensity show a minimal effect of curvature relative to the plane channel.

Like the axial (streamwise) one-dimensional spectra, the temporal spectra of the wall pressure fluctuations of the transversely curved flows also decreases as the curvature increases. A new curvature dependent timescale which increases with increasing curvature was proposed. When scaled with the mean wall shear and this timescale the temporal spectra of the wall pressure fluctuations of the two transversely curved flows studied and that of the plane channel collapse in the high-frequency range.

The two-dimensional spectra and space–time correlations of the wall pressure fluctuations give a lower convection velocity ($U_c \approx 0.6U_\infty$) than in the plane channel. With this convection velocity Taylor's hypothesis holds in the two transversely curved flows studied.

REFERENCES

BLAKE, W. K. 1986 *Mechanics of Flow-Induced Sound and Vibration.* Academic.

CHOI, H. & MOIN, P. 1990 On the space–time characteristics of the wall pressure fluctuations. *Phys. Fluids* A **2**, 1450–1460.

CORCOS, G. M. 1964 The structure of the turbulent pressure field in boundary-layer flows. *J. Fluid Mech.* **18**, 353–378.

ECKELMANN, H. 1989 *Near-Wall Turbulence* (ed. S. J. Kline & N. H. Afgan). Hemisphere.

EMMERLING, R., MEIER, G. E. A. & DINKELACKER, A. 1974 *AGARD Conf. Proc. no. 131 on Noise Mechanisms* **24**, 1–12.

HANDLER, R. A., HANSEN, R. J., SAKELL, L., ORSZAG, S. A. & BULLISTER, E. 1984 Calculation of the wall-pressure field in a turbulent flow. *Phys. Fluids* **27**, 579–582.

KIM, J. 1989 On the structure of the pressure fluctuations in simulated turbulent channel flow. *J. Fluid Mech.* **205**, 421–451.

KIM, J., MOIN, P. & MOSER, R. D. 1987 Turbulence statistics in fully developed channel flow at low Reynolds number. *J. Fluid Mech.* **177**, 133–166.

KRAICHNAN, R. H. 1956 *J. Acoust. Soc. Am.* **28**, 378.

NEVES, J. C., MOIN, P. & MOSER, R. D. 1992 Numerical study of axial turbulent flow over long cylinders. *Rep. TF-54, Department of Mechanical Engineering, Stanford University, Stanford, CA 94305.*

NEVES, J. C., MOIN, P. & MOSER, R. D. 1994 Effects of convex transverse curvature on wall-bounded turbulence. Part 1. The velocity and vorticity. *J. Fluid Mech.* **272**, 349–381.

PANTON, J. L. & LINEBARGER, J. H. 1974 Wall pressure spectra calculations for equilibrium boundary layers. *J. Fluid Mech.* **65**, 261–287.

WILLMARTH, W. W. 1975 Pressure fluctuations beneath turbulent boundary layers. *Ann. Rev. Fluid Mech.* **7**, 13.

WILLMARTH, W. W., WINKEL, R. E., SHARMA, L. K. & BOGAR, T. J. 1976 Axially symmetric turbulent boundary layers on cylinders: mean velocity profiles and wall pressure fluctuations. *J. Fluid Mech.* **76**, 35–64.

WILLMARTH, W. W. & WOOLDRIDGE, C. E. 1962 Measurements of the fluctuating pressure at the wall beneath a thick turbulent boundary layer. *J. Fluid Mech.* **14**, 187–210.

WILLMARTH, W. W. & YANG, C. S. 1970 Wall pressure fluctuations beneath turbulent boundary layer on a flat plate and a cylinder. *J. Fluid Mech.* **41**, 47–80.

WILLS, J. A. B. 1964 On convection velocities in turbulent shear flows. *J. Fluid Mech.* **20**, 417–432.

WILLS, J. A. B. 1970 Measurements of the wave-number/phase-velocity spectrum of wall-pressure beneath a turbulent boundary layer. *J. Fluid Mech.* **45**, 65–90.